ADVANCING EARTH AND SPACE SCIENCES

JGR Earth Surface

RESEARCH ARTICLE

10.1029/2025JF008631

Emergent Dynamics From a Position-Based Calving Function and the Limits of a Rate-Based Calving Function

Iain Wheel[1,2], Douglas I. Benn[1], and Anna J. Crawford[2]

[1]School of Geography and Sustainable Development, University of St Andrews, St Andrews, UK, [2]Division of Biological and Environmental Sciences, University of Stirling, Stirling, UK

Key Points:

- Both steady state and transient glacier behavior emerge from the position-based crevasse-depth calving function
- A calving-rate function fails to capture evolving glacier dynamics
- Assessment of calving functions should include approaches beyond simply tuning to observed changes in terminus positions

Supporting Information:

Supporting Information may be found in the online version of this article.

Correspondence to:

I. Wheel,
iain.wheel@stir.ac.uk

Citation:

Wheel, I., Benn, D. I., & Crawford, A. J. (2026). Emergent dynamics from a position-based calving function and the limits of a rate-based calving function. *Journal of Geophysical Research: Earth Surface*, *131*, e2025JF008631. https://doi.org/10.1029/2025JF008631

Received 3 JUN 2025
Accepted 6 JUN 2026

Abstract

A wide range of functions are currently available for simulating the calving of marine-terminating glaciers, but there is no consensus on the best approach to represent the calving process in glacier and ice-sheet models. Current assessments of calving functions are often crudely done by fitting functions to observed changes in terminus positions, neglecting the physical processes that drive changes in calving dynamics. Here, we use 3D simulations of synthetic tidewater glacier domains in Elmer/Ice, to determine whether natural behaviors emerge from the crevasse-depth and von Mises calving functions, and to provide a basis for more robust assessments of the potential capabilities of calving functions. The crevasse-depth calving function is shown to be able to simulate both serac and full-thickness calving events and simulates how their relative proportion is altered by changing the ice freeboard or submarine melting. A clear distinction between rate- and position-based calving is shown, with the von Mises calving function unable to respond to imposed changes in topography or freeboard ice. By comparing the two calving functions, it is apparent that the position-based crevasse-depth function more faithfully represents the calving behaviors observed in the natural world. Consequently, future projections should be made using position-based calving functions. Using a position function, calving rates vary with time and glacier state, so cannot be assumed to be a constant function of stress. In essence, a calving function must be able to capture the key physical processes that drive calving. If so, the transitions in calving dynamics will inherently emerge.

Plain Language Summary

Calving, the breakoff of iceberg from glaciers flowing into the sea, creates one of the largest uncertainties in future ice-sheet predictions. Glacier models use parameterizations known as calving functions to predict calving processes. Most calving functions used in ice-sheet models are "rate functions" where calving is applied as an ablation rate. These require case-by-case tuning to simulate changing glacier dynamics. Alternatively, calving can be predicted using a "position-based function" where a new location of the glacier terminus is predicted. We conduct a series of experiments using a state-of-the-art 3D model on synthetic domains representing Greenlandic tidewater glaciers to show how both steady state and transient glacier behavior emerge spontaneously from a position-based calving function, and that calving rates are strongly dependent on both the ice flux and the dynamic state of the glacier. Furthermore we extend these tests using a popular rate-based function which fails to detect changes in calving dynamics. Current rate-based calving functions cannot form the basis of reliable predictions, and we propose three standards to assess the validity of a given calving function.

1. Introduction

Calving remains one of the largest sources of uncertainty in future sea level rise projections through ice discharge and iceberg calving from the Greenland and Antarctic ice sheets (IPCC, 2023). Despite recent advances in understanding the relationship between ice dynamics and calving processes (Benn & Åström, 2018), there remains no reliable general "calving law" for use in the continuum models used to predict future evolution of ice sheets. The complexity of tidewater glacier systems makes disentangling the controls on calving such as local topography (Benn et al., 2023; Todd et al., 2018), submarine melting (O'Leary & Christoffersen, 2013) or the presence of a proglacial ice mélange (Cassotto et al., 2021) difficult. However, it remains imperative that the influence of these processes is synthesized into a generic parameterization of calving for long-term projections.

Despite the complexity of calving events, emergent patterns can be recognised at a range of scales that can be used to test predictions of calving models. First, calving styles can be classified into smaller serac calving events - formed from the fracture or collapse of the ice cliff—and larger full-thickness calving events produced from fracture through the entire ice column (e.g., Bézu & Bartholomaus, 2024; Goliber & Catania, 2024). Serac calving is typically a consequence of melt undercutting or flow deformation leading to an unstable overhang, while full-thickness calving events are a result of stress patterns at the ice-tongue scale leading to the release of large icebergs from glaciers or ice shelves. Second, collectively, calving events are observed to have distinctive size distributions (Benn et al., 2026) that conform with fracture theory (Åström et al., 2021; Equation B1). Serac calving events have power-law distributions consistent with self-organizing criticality (Åström et al., 2013; Vallot et al., 2019), while full-thickness events follow exponential distributions reflecting underlying probabilities of calving (Åström et al., 2021; Benn et al., 2026). Third, tidewater glaciers and ice shelves commonly stabilize at locations where lateral and/or basal drag are high (pinning points), and long-term change can be characterized as periods of relative stasis interspersed with episodes of rapid transition (Benn et al., 2023, 2026; Fried et al., 2018; Wheel, Crawford, & Benn, 2024).

There are a wide range of calving models from detailed discrete element models that simulate the realistic patterns of fracture from first principles to continuum models where the ice is represented as continuous medium (Åström et al., 2013; Bondzio et al., 2016). Between these two extremes, there is a host of hybrid methods that explore crevasse propagation or damage evolution (e.g., Duddu et al., 2020; Huth et al., 2021; Mercenier et al., 2019; Sun et al., 2017; Wolper et al., 2021; Zarrinderakht et al., 2024). The continuum models used to predict long-term ice-sheet evolution cannot explicitly model fracture and instead employ a simple calving function, often referred to as a "calving law," to specify the location of the calving front.

Calving functions can be subdivided into two categories: (a) rate-based functions that determine the speed at which ice is removed, which are applied as an ice-loss flux, and (b) position-based functions that determine the location beyond which ice is lost based on the principle that fracture occurs at areas of high stress. Rate-based functions are widely implemented in ice-sheet models as they provide simple, compact functions that are easily adjustable to produce uncomplicated terminus geometries (e.g., Choi et al., 2018; Wilner et al., 2023). Current examples include the von Mises (VM) calving function (Morlighem et al., 2016); eigencalving (Levermann et al., 2012) or prescribed retreat rates based on observations. Position-based functions include the crevasse-depth (CD) (Benn et al., 2007; Nick et al., 2010) and height above buoyancy functions (Vieli et al., 2001), but to date have not been widely implemented in ice-sheet models. However, despite the additional challenges involved in their implementation, increasing evidence suggests that position-based calving functions more faithfully reflect the way that full-depth calving actually works (e.g., Benn et al., 2023; Todd et al., 2018; Wheel, Crawford, & Benn, 2024). Damage-based modeling adds further agreement that calving is best replicated using fracture locations as parameterized by position-based functions rather than an ice-flux loss as is implemented by rate-based functions (Huth et al., 2023; Ranganathan et al., 2025). That is, calving occurs at a particular location due to local stress regimes, and the velocity only influences how fast ice reaches this location rather than being directly related to the calving dynamics (Benn et al., 2023; Crawford et al., 2024).

Despite the important debate about calving functions for ice-sheet models, the ways that they represent calving dynamics are rarely considered. Usually, calving-function evaluation involves the imprecise manual adjustment of the calving parameterization to fit observed terminus position change at a given location (e.g., Choi et al., 2018; Wheel, Crawford, & Benn, 2024), which we refer to as 'tuning'. To move the calving function debate forward we directly compare popular rate- and position-based calving functions. We show that the capabilities of calving functions can extend far beyond simple matching of observed rates of change, and can include the three emergent behaviors identified above: calving styles, calving size distributions, and ice-front stabilization and transition. Together, these behaviors provide a more robust framework to assess calving functions.

2. Methods

The open-source 3D Stokes finite element model Elmer/Ice (Gagliardini et al., 2013) is used for all experiments. Elmer/Ice is capable of solving a multitude of glaciological problems including the grounding contact problem (Favier et al., 2012) and ice temperature evolution (Gagliardini et al., 2013). We use the calving algorithm presented in Wheel, Benn, et al. (2024) to implement calving. The model presented in Wheel, Benn, et al. (2024) uses the CD calving function to predict the location of calving events based on computed tensile principal stress (Benn et al., 2007; Nick et al., 2010; Todd et al., 2018). The "crevasse" envelope is represented as

$$\sigma_{p,surf} = \sigma_1, \tag{1}$$

$$\sigma_{p,basal} = \sigma_1 + P_w, \tag{2}$$

where σ_1 is the largest principal stress and P_w is the water pressure at basal crevasses and is calculated following Todd et al. (2018). In the Wheel, Benn, et al. (2024) model, calving occurs down the vertical plane, but the terminus of the glacier is free to evolve in any direction due to glacier flow or melting. Thus, calving events less than the terminus thickness can be produced for overhanging and undercut calving faces or those with a buoyant foot. For these scenarios, calving down the vertical plane can intersect the calving face, thereby producing small or serac events. Additionally, we implement the rate-based von Mises calving function first presented by Morlighem et al. (2016) for a 2D model as

$$c = |\mathbf{v}|\frac{\tilde{\sigma}}{\sigma_{\max}} \tag{3}$$

where c is the calving rate, $\mathbf{v}$ is terminus velocity vector, $\tilde{\sigma}$ is the von Mises stress and $\sigma_{\max}$ is the tensile stress threshold. In the Elmer/Ice implementation, the von Mises stress on the calving face, $\tilde{\sigma}$, is calculated directly from the full Cauchy stress tensor as the glacier dynamics are solved in 3D. Trials were run using a fully 3D implementation where $\tilde{\sigma}$ is a 2D field across the calving face as the Wheel, Benn, et al. (2024) algorithm can accept complex 3D calving predictions. However, it became clear because the VM calving function was originally conceived as a 2D function, it could not replicate serac calving events. The increased overhanging led to element degeneracy over time. Therefore, we use a vertically integrated mean value of $\mathbf{v}$ and $\tilde{\sigma}$ to prevent distortion of the terminus.

The complete domain setup (Figure 1) with the associated boundary conditions is outlined in Appendix A. The domain represents a typical tidewater glacier flowing on a prograde slope with narrowing fjord margins (Figure 1). Two basal rises with a width of 550 m and a maximum height of 100 m are present near the terminus. A central plume with a maximum melt of 500 m a^{-1} is prescribed, with low background melt across the remaining submerged terminus. The mesh resolution is maintained at 50 m vertically and horizontally at the terminus to produce a high resolution result. A synthetic geometry is used for several key reasons: (a) a simple domain can be easily manipulated geometrically or through the boundary conditions to highlight key drivers of calving; (b) real world 3D domains such as those at Store Glacier (Sermeq Kujalleq) (Todd et al., 2018) and Jakobshavn Isbrae (Sermeq Kujalleq) (Wheel, Crawford, & Benn, 2024) produce very complex dynamics which require interpretation as opposed to simple, unambiguous synthetic domains; and (c) the central aim of this study is to highlight what calving processes can be captured by continuum calving functions. This is best done when calving functions are not tuned to match observations and rather the tuning becomes an arbitrary factor. To provide a comparison between rate- and position-based calving functions, control experiments are run with both the VM and CD functions. For the CD function the crevasse penetration threshold for calving is set to 92.5% and for the VM function $\sigma_{\max}$ is set to 300 kPa with both of these parameters matching simulations at real world glaciers (e.g., Choi et al., 2018; Wheel, Crawford, & Benn, 2024; Wilner et al., 2023). The final terminus position of both control experiments was very similar (Figure 2).

To assess the performance of the both the rate-based VM function and position-based CD function, we alter either the physical characteristics of the domain or the boundary conditions applied. We run two sets of experiments: those with a defined initial geometry (referred to as stability experiments) and those with a relaxed domain (referred to as relaxed experiments). The stability experiments are run for 100 days. In the first round of experiments the ice freeboard of the starting domain is altered. The ice freeboard at the terminus is set to 50 m in the control and further experiments were conducted with 40, 45, 55, and 60 m ice freeboards where the ice freeboard is S_0 in Equation A7. The gradient of the ice surface remained constant. Next, experiments were conducted by altering the inflow velocity that was set to 1,000 m a^{-1} for the control. Simulations were run with inflow velocities of 500 m a^{-1}, 750 m a^{-1}, 1,500 m a^{-1}, 2,000 m a^{-1}. Two rounds of experiments were conducted using either altered fjord or basal geometry. The setup fjord geometry was altered by moving the straightening of the fjord walls further upstream. The basal geometry of each experimental setup was altered by moving the two basal rises present near the terminus further upstream. For each the geometric feature (the fjord walls or the basal rises) was moved 250, 500, 750, and 1,000 m upstream (Figure 1e). The penultimate set of experiments added a mélange back pressure to the top 100 m of the terminus below the waterline. The mélange was present between days 10 and

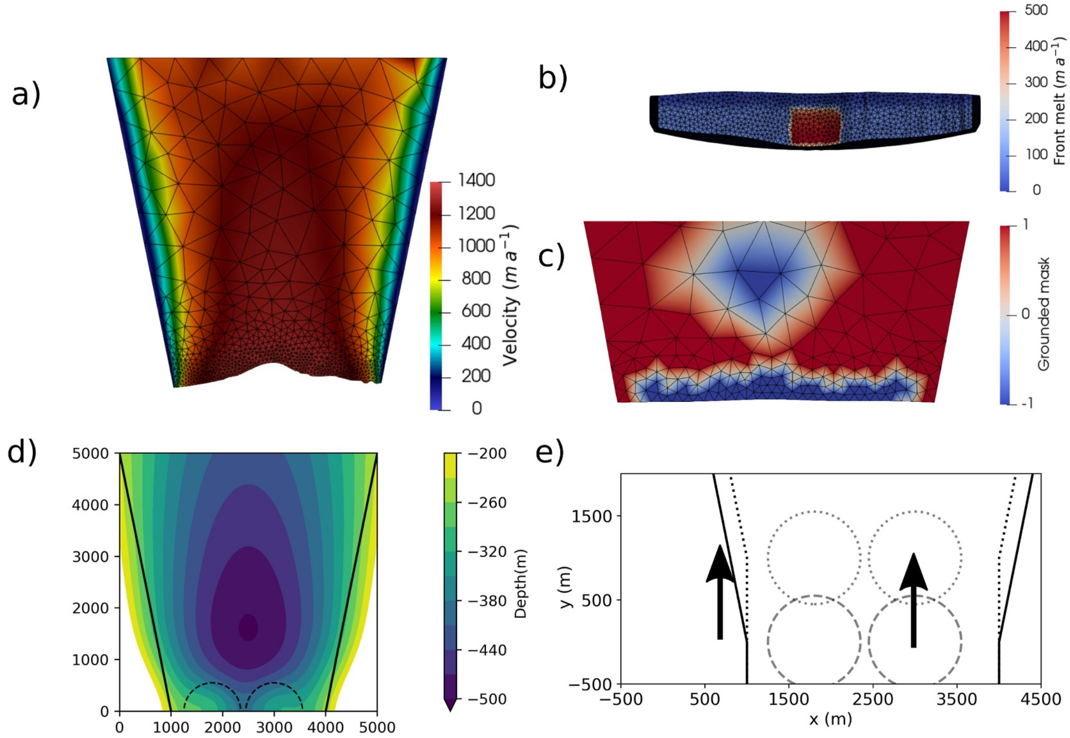

Figure 1. The synthetic geometry setup. (a) Topdown view of the mesh at the end of the 100 day control experiment. Horizontal mesh element size is 50 m at the terminus and increases to 500 m further upstream. The velocity field is displayed. (b) Front view of the same mesh displaying the horizontal and vertical mesh element size of 50 m. The submarine melt is displayed showing the meltwater plume in the center. (c) Topdown view of the base boundary elements displaying the initial grounding zone. Values of 1 indicate grounded elements and values of −1 indicate ungrounded elements. (d) The bed geometry displaying the basal rises - outlined by the dotted line - and the lateral margins - shown by the solid black lines. (e) The control and end members of the domain for the geometric experiments. The solid black lines show the fjord walls. The dotted black lines showing the end member where the fjord wall straightening has been moved 1,000 m upstream. The two gray dashed circles indicate the control position of the extent of the basal rises. The gray dotted circles show the end member where the basal rises have been moved 1,000 m upstream. The arrows indicate the movement of the geometric features upstream.

80 and experiments were run with contact pressures of 72, 144, 216, and 288 kPa. For the final set of experiments the submarine melt from central plume was extended across the whole width of the glacier terminus. In the control the plume was only 500 m wide with a maximum melt of 500 m a^{-1}. The plume profiles were then normalized against maximum melt rates of 250 m a^{-1}, 375 m a^{-1}, 500 m a^{-1}, 750 m a^{-1}, and 1,000 m a^{-1}. No melt

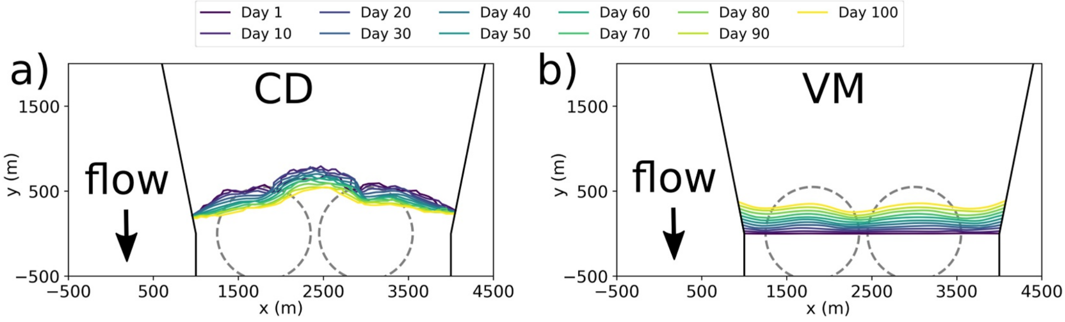

Figure 2. Terminus positions through time for the control experiments with (a) the crevasse-depth (CD) and (b) the von Mises (VM) calving functions. The black lines indicate the fjord walls which act as the lateral constraints to the glacier. The gray dashed lines outline the basal rises. The full bed geometry is provided in Appendix A.

undercutting experiments were performed using the VM function since it relied on vertically integrated mean terminus values so melt is constant with respect to the z-coordinate.

The relaxed experiments use the same initial setup but with the addition of 5 year transient relaxation of surface and base free surfaces. The relaxed domain is used as the starting point for a series of 5-year experiments. The first set has an annual mélange backstress with a contact pressure of 144 kPa applied between days 120–240 of each year. The second set had a varying inflow velocity reaching a peak at 1,500 m a^{-1} at the start of each year and a minimum of 500 m a^{-1} at the midpoint of each year. For the final set of experiments, these inflow conditions are repeated but the initial geometry is altered by moving the basal rises upstream 250 m prior to the relaxation. For the relaxation experiments, the crevasse penetration threshold in the CD function is set to 82.5% (as used in Benn et al., 2026). For the VM function, $\sigma_{\max}$ is set to 650 kPa, which is well within the values used at real glaciers (e.g., Choi et al., 2018; Wilner et al., 2023). Using the full stress tensor, more shear is modeled in the margins causing the VM function to remove the glacier shear margins in the first year of a simulation. We therefore limit $\tilde{\sigma}$ to 650 kPa.

3. Results

3.1. Control

In the control experiment using the CD function the glacier underwent immediate rapid retreat before stabilizing and advancing on basal rises present for the remainder of the simulation whereas the VM control experiments retreated in a linear manner (Figure 2). Consequently for the CD control, the largest daily calving volume was within the first few days (Figure 3c) before reducing as the terminus stabilized. After 40 days, the daily calving volume began to fluctuate between almost no calving and a daily calving volume of 4×10^6 m^3. These changes are further illustrated using the cumulative calving volume, where the gradient of volume change is the volumetric calving rate (Figure 3d). Three periods of consistent calving rates can be seen (Figure 3d). The first, very high calving rate, occurred immediately during the rapid transition to a stable position. The second occurred as the glacier stabilized on the pinned location. Once the glacier front has become stable, the final calving rate relates directly to the velocity, or the rate at which ice is delivered to the stable position. The calving volume for the control experiment using the VM calving function increased slightly through time (Figure 3c) producing a near linear increase in the total calving volume (Figure 3d). As the calving rate was near uniform a very narrow range of calving event sizes were produced (Figure 3a).

Calving size distributions from the CD function showed similarities to those proposed using fracture theory by Åström et al. (2021) (Figure 3a; Appendix B). The modeled calving size distributions reflect calving from a wide range of calving styles with smaller events ($<10^5$ m^3) from serac style calving and larger events ($>10^5$ m^3) from full-thickness calving. Very large events ($>10^8$ m^3) were produced at the start of the simulation while the glacier was retreating rapidly to a stable position. The VM function produced a very narrow distribution with icebergs sizes between 10^6 m^3 and 10^8 m^3.

3.2. Ice Freeboard

When using the CD function, reducing the ice freeboard increased the retreat of the glacier by producing more calving: predominantly full-thickness buoyant calving (Figure 4). Apart from the case with the smallest ice freeboard, all the simulations remained pinned on the basal rises. For the simulation with the lowest ice freeboard, the glacier retreated further upstream than the basal rises. All the simulations showed a similar pattern of the total calving volume through time to the control experiment, with a rapid initial increase in volume (high calving rate) before stabilizing and increasing linearly once the terminus had stabilized, with a calving rate determined by the inflow velocity.

The calving size distributions showed several distinct changes as the ice freeboard of the glacier setup was altered (Figure 4b). First, the experiment with the smallest ice freeboard showed a large increase in both larger and very large events from full-thickness calving (Figure 4c). Conversely, the experiment with increased ice above the waterline had more calving events around 10^5 m^3 in volume, associated with an increase in serac calving events. Very small calving size distributions were similar for all the simulations.

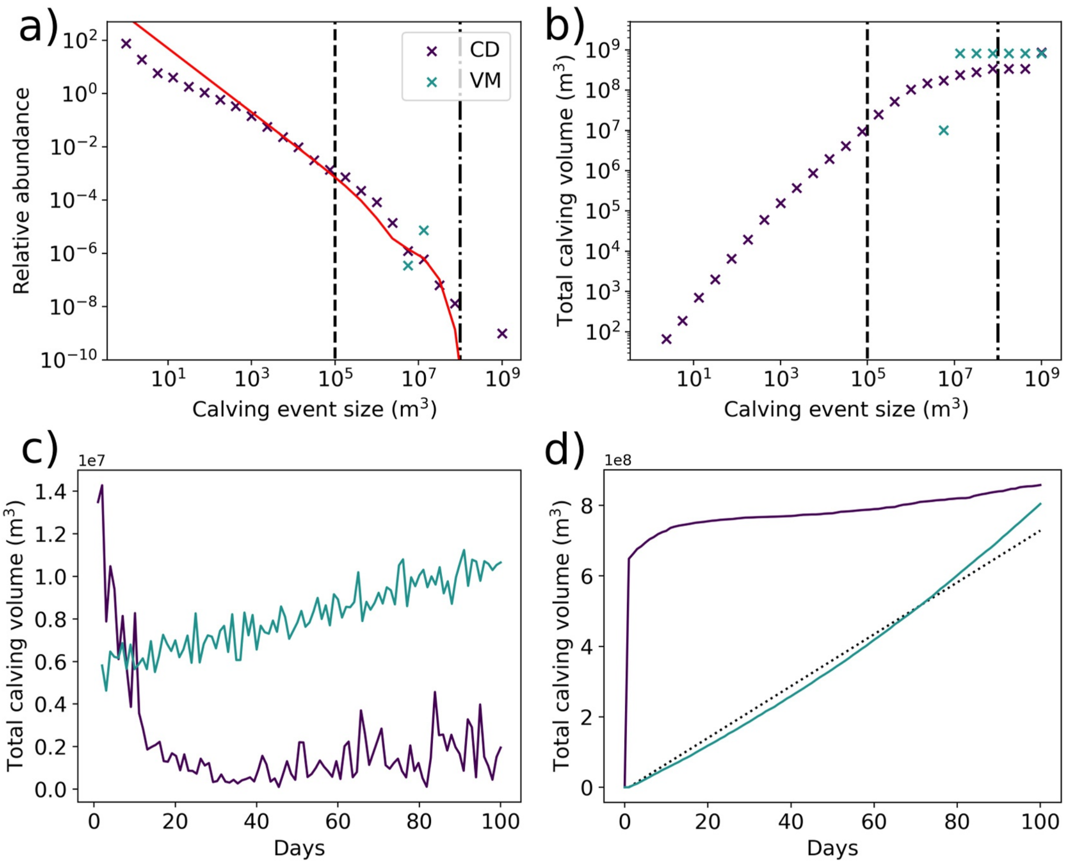

Figure 3. The calving output from the control experiments for both the crevasse depth (CD) and von Mises (VM) calving functions. (a) The calving size frequency distributions with the solid red line showing the theoretical fracture distribution from Åström et al. (2021) with values of 1.2 (α), 800 (c_1), 2.5 × 10^{-6} (c_2), 10^6 (S_2), 10^7 (S_2) in Equation B1. (b) Total calving volume for each calving size distribution. The dashed lines indicate the divide between small events from serac calving (<10^5 m^3), larger events (>10^5 m^3) and very large events (>10^8 m^3) from full-thickness calving. (c) The daily calving volume through time. The first day is not displayed as it would dominate the plot. (d) Total calving volume for the control simulations through time. The gradient of the line is the equivalent to the calving rate. The black dotted line represents the estimated inflow volume.

Conversely, the VM function showed limited changes against the control with alterations in ice freeboard (Figure 4b). Increased ice freeboard, in contrast to the CD function, led to fractionally more calving as higher ice cliffs slightly raised $\tilde{\sigma}$ (Figure 4d).

3.3. Inflow Velocity

When using the CD function, experiments run using a modified inflow velocity boundary condition all stabilized at the same location on the basal rises (Figure 5a). Differences were seen in the central portion of the glacier between the basal rises where the melt water plume was applied. Here, faster flowing glaciers advanced further as the submarine melt to velocity ratio decreased. Additionally, as the location of the advance lies between the basal rises, it is not pinned by the basal topography.

Increased velocity led to an increase in larger calving events (Figure 5c) while the number of smaller calving events remained constant between simulations. Regardless of velocity, there was a period of rapid adjustment as the glacier stabilized on the pinned location (Figure 5d). Greater velocities produced higher calving volumes but the pattern of the adjustment period of the glacier, and so the initial calving rate, was identical. Once the terminus was stable after 40 days the total calving volumes increased near linearly with a slight acceleration through time. The stable calving rate, defined as the gradient of the linear increase, was directly proportional to the inflow velocity condition applied, with higher velocities producing a steeper increase in total calving volume.

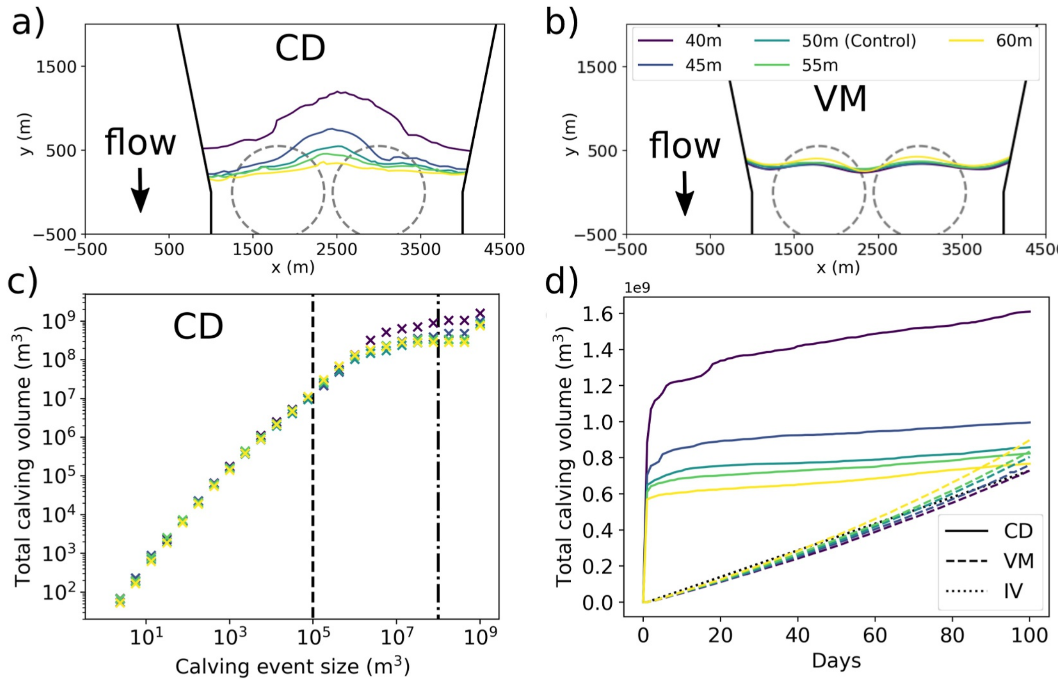

Figure 4. Terminus positions and calving outputs for the ice freeboard simulations for both the crevasse depth (CD) and Von Mises (VM) calving functions. (a) Terminus positions after the 100 day simulations using the CD function. (b) Terminus positions after the 100 day simulations using the VM function. The legend denotes the ice freeboard present at the terminus for each setup for all panels. (c) Total calving volumes for each size distribution using the CD function. The dashed lines indicate the divide between small events from serac calving ($<10^5$ m^3), larger events ($>10^5$ m^3) and very large events ($>10^8$ m^3) from full-thickness calving. (d) Total calving volume through time using the CD (solid lines) and VM (dashed lines) calving functions. The dotted line (IV) is the estimated inflow volume.

Unlike the CD function, terminus positions in experiments using the VM were highly dependent on the glacier velocity with increasing velocity producing a higher calving rate (Figure 5b). Simulations also showed a velocity dependency feedback where increased velocity, increased retreat and so led to an increased velocity and retreat rate (Figure 5d).

3.4. Geometry

The lateral and basal geometries were altered independently to test their influence on calving. For the CD function, upglacier shifting of the straightening of the lateral margins caused the terminus position to correspondingly migrate further upstream (Figure 6a). Likewise, the shifting of the basal rises further upstream resulted in the terminus moving upstream (Figure 7a). For both series of experiments the relocation of the terminus further upstream occurred rapidly near the start of each experiment. Large full-thickness calving events were produced, with the majority of total calving volume produced during this transition (Figures 6 and 7d). The magnitude of the total calving volume was proportional to the distance upstream that the pinning locations and stable terminus had been moved. Initial calving rates were associated with the distance upstream the terminus had to retreat before stabilizing. Following the rapid transition to the stable position, the glacier remains stable and the calving volume increases linearly, and the gradient of the linear slope (i.e., the volumetric calving rate) is identical for all simulations. The one exception is the 1,000 m lateral geometry simulation where a higher calving rate was present at the end of the experiment. Here, the glacier continues to retreat after the transition period as it becomes unpinned from the basal rises.

Higher numbers of full-thickness calving events are seen as the stable position is moved further upstream (Figures 6 and 7c). These are produced as the glacier transitions to a stable position. Calving size distributions of smaller events remain roughly equivalent between the geometric simulations.

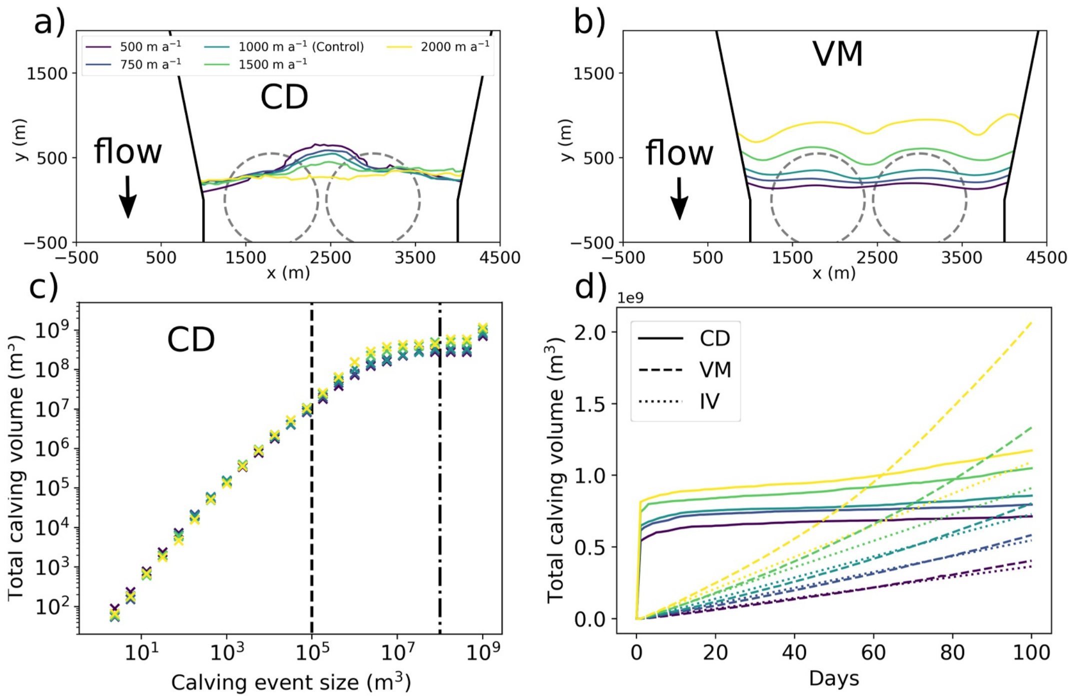

Figure 5. Terminus positions and calving outputs for the velocity simulations using the crevasse depth (CD) and von Mises (VM) calving functions. Terminus positions after the 100 day simulations using the (a) CD and (b) VM calving functions. (c) Total calving volumes for each size distribution using the CD function. The dashed lines indicate the divide between small events from serac calving (<10^5 m^3), larger events (>10^5 m^3) and very large events (>10^8 m^3) from full-thickness calving. (d) Total calving volume through time using the CD (solid lines) and VM (dashed lines) calving function. The dotted lines (IV) are the estimated inflow volume.

The same experiments run using the VM function showed no dependency on either the lateral (Figure 6b) or bed topography (Figure 7b). The slight differences in calving volumes seen when the basal rises are moved upstream is a consequence of minor increases in the terminus velocity in the absence of pinning points rather than a direct response to geometric change (Figure 7d). Similarly, when the fjord is straightened further upstream, the reduction in terminus width decreases the calving volume slightly, despite the parallel margins producing less buttressing to the terminus.

3.5. Mélange

When using the CD function, the final terminus position of the simulations was independent of the seasonal mélange back stress applied between days 10 and 80 (Figure 8). The final position remains similar to that of the control when no mélange was present. However, when the mélange backstress was present the calving rate was reduced (Figure 8d). Stronger mélange backstress produced less calving while present, allowing the terminus to move further down-fjord. Irrespective of the prescribed mélange backstress, once removed the terminus rapidly retreats to the stable position occupied by the control. After mélange removal, a higher calving rate produced a rapid increase in calving volume, trending toward that of the control. The calving size distributions showed a clear pattern when mélange backstress was increased. Smaller serac events (<10^5 m^3) and smaller full-thickness events (10^5–10^6 m^3) reduced with an increase in mélange backstress. Conversely, larger full-thickness events (10^7–10^8 m^3) increased in the period after the removal of a strong mélange. Very large events (>10^8 m^3) were unchanged between the simulations.

The VM function showed a modest decrease in calving rate when a mélange backstress was applied but there was no increase in calving following the removal of the mélange (Figure 7). Calving rates remained near constant throughout the simulation. Although the calving volumes by the end of the CD and VM experiments are roughly equivalent, the calving rates through time are entirely different. The CD function shows a reduction when the mélange is present, while for the VM experiments the calving rates are near constant.

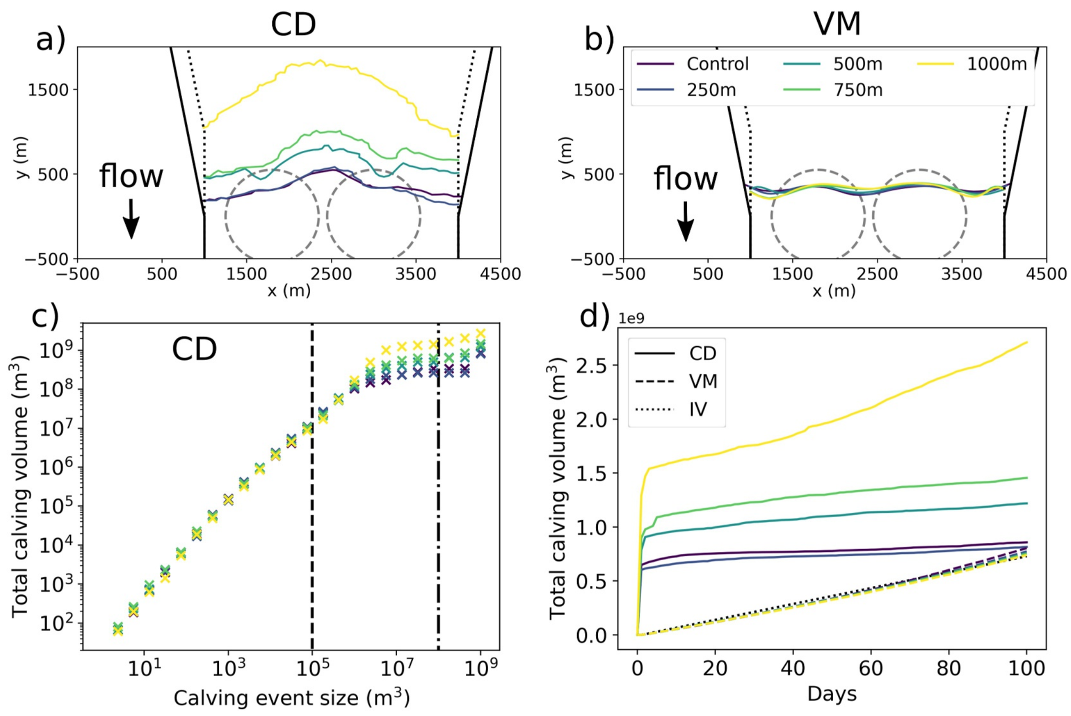

Figure 6. Terminus positions and calving outputs for the altered lateral geometry simulations using the crevasse depth (CD) and von Mises (VM) calving functions. Terminus positions after the 100 day simulations for (a) CD and (b) VM calving functions. The two end members of the simulations are shown with the control lateral margins shown by the solid black line and the lateral margins moved 1,000 m upstream shown by the dotted black line. (c) Total calving volumes for each size distribution using the CD function. The dashed lines indicate the divide between small events from serac calving ($<10^5$ m^3), larger events ($>10^5$ m^3) and very large events ($>10^8$ m^3) from full-thickness calving. (d) Total calving volume through time for CD (solid lines) and VM (dashed lines) calving functions. The dotted line (IV) is the estimated inflow volume.

3.6. Melt Undercutting

Only the CD function could be tested for the influence on melt undercutting since the VM function relied on vertically integrated values. Increases in terminus-wide submarine melting led to a small incremental retreat of the final terminus position (Figure 9a), although in all simulations the front remains pinned by the basal rises. Serac calving events ($<10^5$ m^3) increased with increased melt undercutting (Figure 9b). However, there was a reduction in full-thickness calving events (10^5–10^7 m^3), resulting in the total calving volume showing no clear pattern with increased melt (Figure 9c).

3.7. Relaxation Experiments

Using the CD function, the terminus rapidly retreated to a stable position, roughly equivalent to where the center of the basal rises was located (Figure 10a). When the annual mélange backstress was applied the terminus advanced before retreating to its original position once the backstress was removed. The annual cycle showed a similar pattern each year. Conversely, the VM function did not display a seasonal cycle or a stable location (Figure 10a). The glacier initially advances as the terminus wants to form a convex shape (the center is more advanced compared the margins) before slowly retreating. When a seasonal inflow variation was applied a similar pattern was observed with limited seasonal changes (Figure 10b). For the same experiment the CD function oscillated around its stable position. For the domain where basal rises had been moved upstream the stable point of the CD function moved further upstream and then oscillated around this position (Figure 10c). When the basal rises had been moved, the VM function showed similar pattern as the VM experiment with no shift in the bedrock. However, it retreated slightly more and showed a slight seasonal pattern with more retreat when the inflow velocity was higher (Figure 10c).

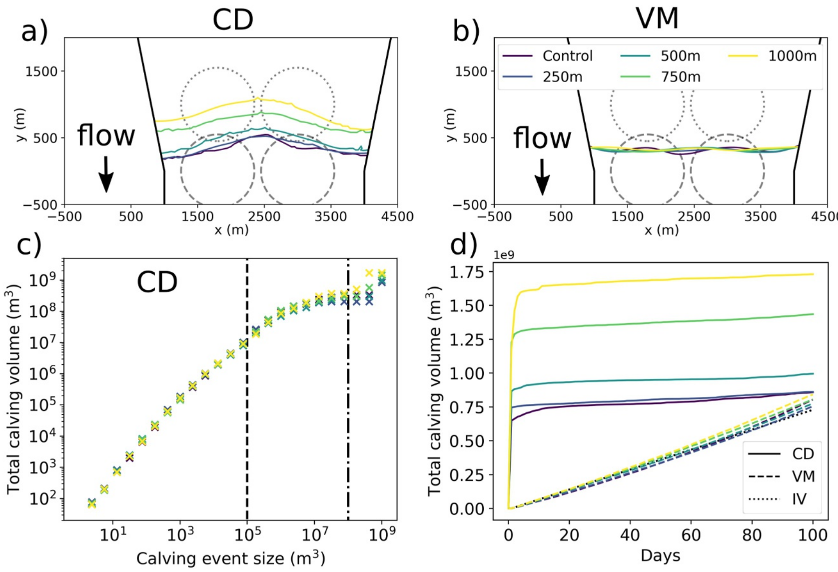

Figure 7. Terminus positions and calving outputs for the altered bed geometry simulations using the crevasse depth (CD) and von Mises (VM) calving functions. Terminus positions after the 100 day simulations for (a) CD and (b) VM calving functions. The end members of the experiments altering the bed geometry are shown with the dashed black line showing the position of the basal rises in the control and the dotted black line showing the position of the basal rises 1,000 m upstream. (c) Total calving volumes for each size distribution using the CD function. The dashed lines indicate the divide between small events from serac calving ($<10^5$ m^3), larger events ($>10^5$ m^3) and very large events ($>10^8$ m^3) from full-thickness calving. (d) Total calving volume through time for CD (solid lines) and VM (dashed lines) calving functions. The dotted line (IV) is the estimated inflow volume.

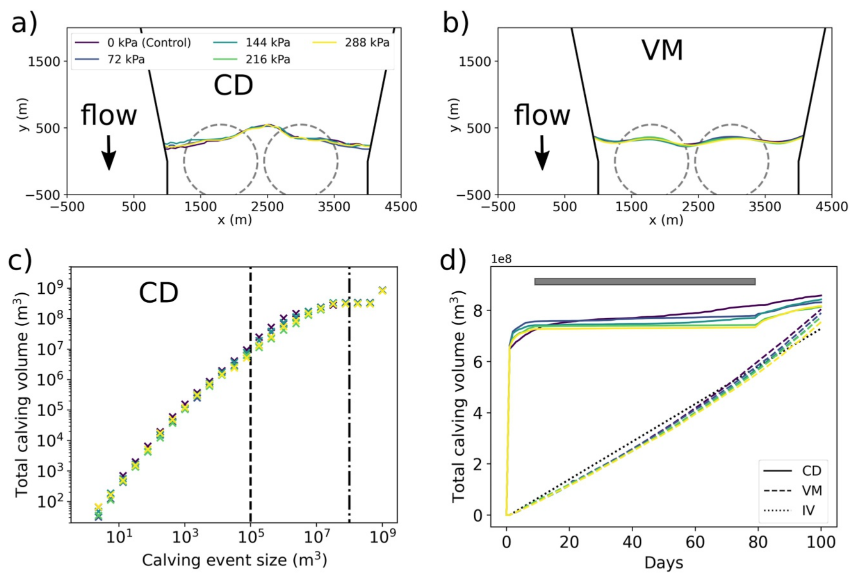

Figure 8. Terminus positions and calving outputs for the mélange simulations using the crevasse depth (CD) and von Mises (VM) calving functions. Terminus positions after the 100 day simulations using (a) CD and (b) VM calving functions. (c) Total calving volumes for each size distribution using the CD function. The dashed lines indicate the divide between serac ($<10^5$ m^3), larger events ($>10^5$ m^3) and very large events ($>10^8$ m^3) from full-thickness calving. (d) Total calving volume through time using the CD (solid lines) and VM (dashed lines) calving functions. The dotted line (IV) is the estimated inflow volume. The gray box from 10d to 80d represents the time period the mélange backstress was applied.

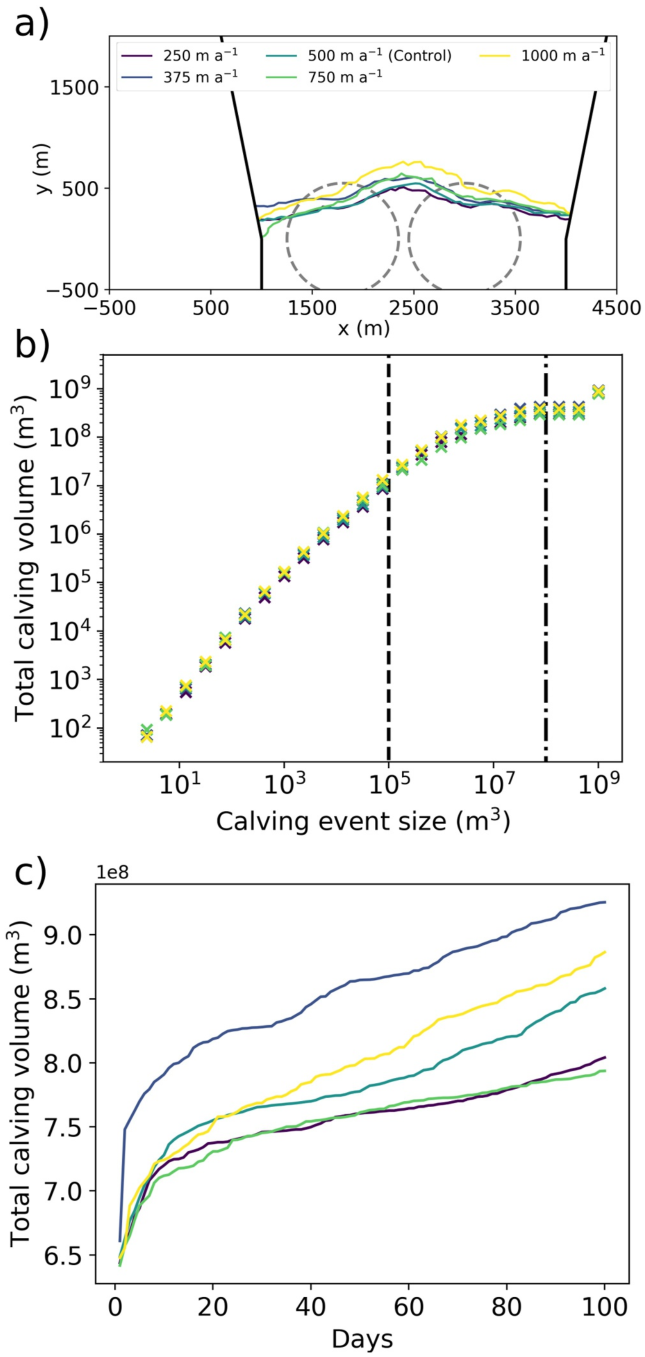

Figure 9. Terminus positions and calving outputs for the submarine melt simulations using the crevasse depth (CD) calving function. (a) Terminus positions after the 100 day simulations. (b) Total calving volumes for each size distribution. The dashed lines indicate the divide between serac ($<10^5$ m^3), larger events ($>10^5$ m^3) and very large events ($>10^8$ m^3) from full-thickness calving. (c) Total calving volume through time. The dotted line is the estimated inflow volume.

4. Discussion

4.1. Calving Rates Through Time

The calving rate, defined here as the rate of the increase of the cumulative calving volume, varied throughout the simulations, depending on the transient state of the glacier when using the CD function, whereas when using the VM function calving rates were near constant (e.g., Figure 3). Using the CD function, the initial unstable geometries produced high calving rates that increased with the distance of the glacier from its stable position (Figure 5). As the terminus stabilized, the calving rate decreased, and once the terminus had stabilized the calving rate was directly proportional to the terminus velocity.

4.2. Shifts in Calving Style

4.2.1. CD Function

The CD function produced both serac and full-thickness calving events, with emergent calving size distributions closely following those identified by Åström et al. (2021): a power law for serac style calving and an exponential distribution for full-thickness calving (Figure 3a; see Equation B1). It is likely that a longer simulation with a seasonal signal would be required to exactly replicate the exact Åström et al. (2021) distributions.

In the stability experiments, by altering the ice freeboard of the glacier setup, we changed the dynamics of the glacier and so altered the dominant calving processes. A smaller ice freeboard favored larger full-thickness calving events although smaller serac events were still occurring (Figure 4). Without changing the calibration of the CD function, changes in glacier dynamics are represented in the simulated calving styles. Similarly, increased melt undercutting produced more serac calving events without altering full-thickness calving (Figure 9).

4.2.2. VM Function

The VM function produced a very limited calving distribution, because it is the nature of a rate-based function to remove small slices from the terminus at each timestep (e.g., Figure 3a). However, given the integrated approach and its original conception for 2D ice-sheet modeling it should be not be expected to display a full range of calving styles including serac calving. Instead, it should be able to detect changes in the glacier dynamics and alter the calving rate accordingly. Concerningly, our experiments show no response to change in lateral or basal topography despite it being widely accepted that local geometry suppress or exacerbate calving through lateral or basal pinning (e.g., Alley et al., 2023; Benn et al., 2023; Todd et al., 2018; Wheel, Benn, et al., 2024). Similarly, unlike the CD function, the VM displays no distinct response to mélange backstress (Figure 8). Finally, the VM function shows no sensitivity to ice freeboard, regardless of how this should increase buoyant full-thickness calving (Figure 4).

Rather, when using the VM function, calving rates only respond directly to changes in terminus velocity. This relationship can be broken down into two possible responses. First, calving applied as a rate is inherently correlated to velocity as it is a term within the calving function. Second and separately, the VM function shows an increasing velocity-calving rate feedback loop (Figure 5). Here, as the terminus velocity increases, the associated $\tilde{\sigma}$ increases faster producing higher calving rates. As the terminus retreats, the glacier accelerates further increasing $\tilde{\sigma}$, and producing the VM velocity-calving rate feedback loop. This feedback is inconsistent with observations.

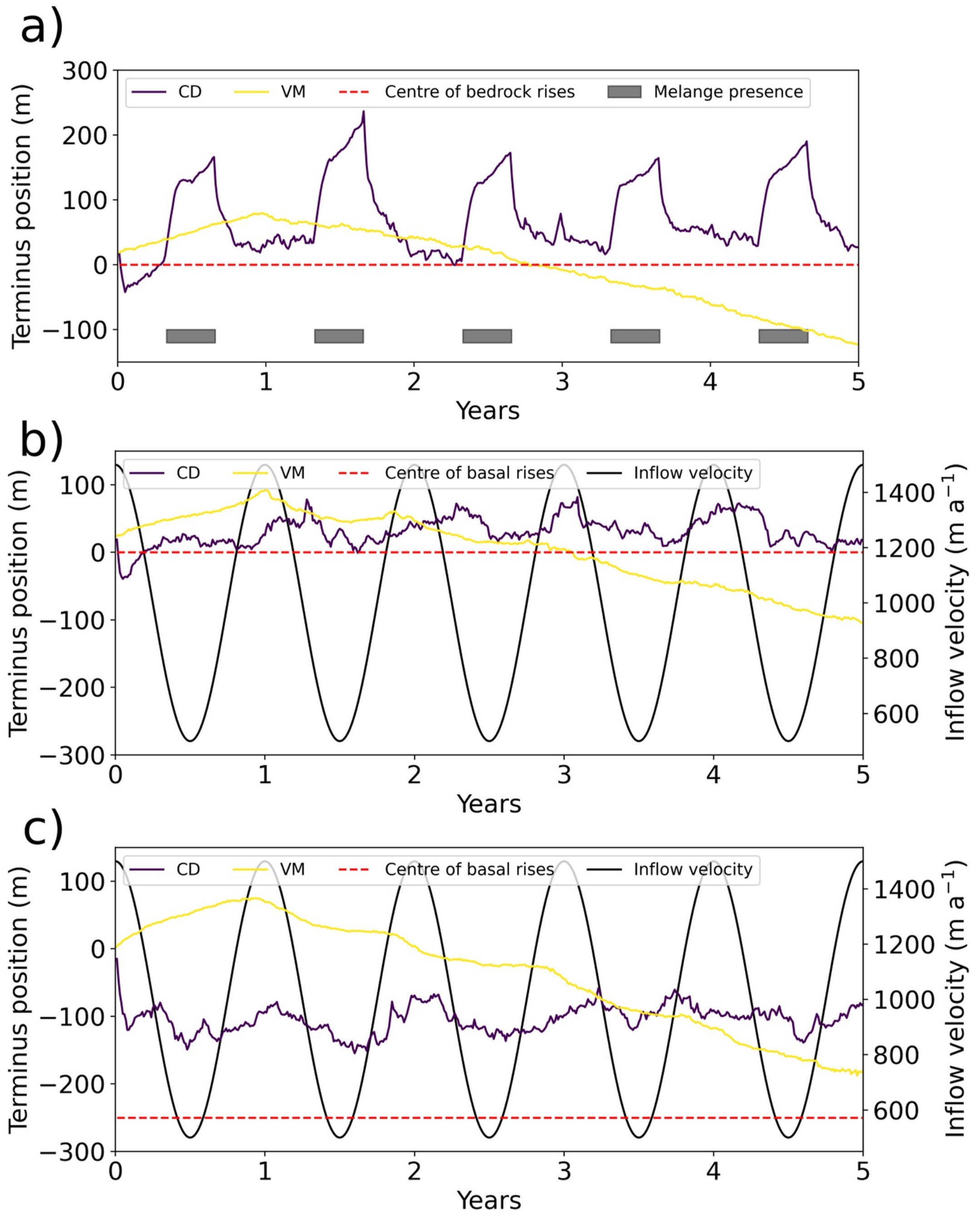

Figure 10. Terminus positions for the series of calving simulations with a relaxed domain. (a) Mean terminus positions when a seasonal mélange is applied. (b) Mean terminus positions when seasonal inflow velocity is applied for (b) the standard setup and (c) when the basal rises have been moved 250 m upstream prior to the relaxation and the transient experiments.

Typically, glaciers rapidly stabilize following a velocity perturbation (e.g., Benn et al., 2026; Bézu & Bartholomaus, 2024; Fried et al., 2018). Therefore, dynamic responses predicted by the VM function should be regarded as a potential model artifacts and treated with caution.

4.3. Calving Stability Dictated by Local Geometry

Previous studies have suggested that calving is dictated by geometry through local changes in the stress field (Benn et al., 2023; Todd et al., 2018; Wheel, Crawford, & Benn, 2024). Despite this, rate-based calving functions have remained the mainstay of ice-sheet and glacier modeling. This study produces evidence that full-thickness calving is governed by the position of regions of high tensile stress, and so terminus locality is independent of velocity. In our simulations with the CD function, increases in the velocity field made no difference to the stable terminus position (Figure 5), while changes in the basal or lateral geometry led to a predictable shift in the stable terminus position (Figures 6 and 7).

The historical confusion over the driver of calving rates stems from the difference between calving volume and terminus location. If the terminus is stable, the calving rate scales directly with terminus velocity as calving occurs at some point beyond the stabilization location. This can be seen in the total calving volume of the last 50 days of the velocity experiments where the gradient of the total calving volume directly relates to the prescribed inflow boundary condition (Figure 5c). Simply, the calving rate equals the rate of ice delivery to the pinning point. However, this relationship has overshadowed the key driver of where the terminus stabilizes, which is illustrated through the first half of the stability inflow velocity simulations (Figure 5c). The stabilization of the terminus is purely dictated by local geometry and entirely independent of the velocity field. Without this component of the calving function, it is impossible to model calving with any form of certainty as the terminus cannot transition between dynamical states. The rate of calving during the transition to a stable state differs from the calving rate once the glacier stabilizes. Rate-based calving functions can only model calving of one glacier state, which is clearly seen in the relaxed experiments. In a longer-term relaxed simulation, when a seasonal inflow velocity is applied, the independence from the velocity is less clear. These experiments illustrate the confusion about whether calving is rate- or position-based process (Figure 10b). Neither the CD nor the VM function clearly displays a seasonal signal. However, when the basal pinning points are moved the terminus should stabilize further upstream and once stabilized, the calving rate becomes the delivery of ice to that location (Figure 10c). The CD experiments transition to different stable locations based on the bed geometry. Conversely, the VM function undergoes the same transient retreat for either setup. When a calving function imposes a calving state onto the glacier, as the rate-based VM function does in our experiments, manual tuning is necessary to show periods of transitions and so are not appropriate for any future projections. We therefore recommend that any continuum calving model use a position-based calving function.

4.4. Seasonal Mélange Does Not Alter Stable Terminus Positions

Another debate about calving dynamics is the possibility that a mélange backstress can stabilize the terminus. A prevalent view is that the position of glacier fronts reflects the balance between summer and winter influences on the calving rate; that is, melt-undercutting causes summer retreat and a cessation of melting and the presence of mélange causes winter advance. According to this view, changes in the balance between melting and mélange backstress will result in changes to the mean annual position of the glacier. This view is well illustrated through the argument by Joughin et al. (2020) that the recent stabilization of Jakobshavn Isbrae's (Sermeq Kujalleq) frontal position was due to the renewed presence of strong winter mélange. However, Wheel, Crawford, and Benn (2024) found that Jakobshavn Isbrae (Sermeq Kujalleq) stabilized at the same position, which related to basal pinning points, regardless of the seasonal ice mélange. Here, we have shown that, when present, the mélange allows the glacier to advance beyond a stable position through the suppression of calving, producing a lower calving rate. When removed, the glacier returns to the same stable position regardless of the magnitude of the mélange backstress (Figure 8). Stronger mélange backstress suppresses serac ($<10^5$ m^3) and small full-thickness events (10^6 m^3). By allowing a greater advance, a stronger mélange backstress leads to more full-thickness calving events when removed as the terminus rapidly retreats to a stable position.

Even over the multiyear relaxed experiment seasonal mélange cannot alter the location of stable terminus positions (Figure 10a). The summer stable terminus position is unaffected by the presence of winter mélange. However, it is likely that prolonged mélange presence may allow the glacier to readvance downstream to a new stable position although to date no clear observational evidence has been provided for this.

4.5. Calving Is a Stabilization Process

One of the major considerations when producing glacier simulations is the model spinup procedure. In simulations of real-world glaciers, domain relaxations are often undertaken to remove any potential mismatches between the domain and glacier flow solution. Relaxation of a domain potentially alters the calving directly though changing the glacier geometry or indirectly through modification of either the velocity or stress field. Unrelaxed geometries can potentially be criticized for being unphysical. However, regardless of whether a geometry could exist in the natural world, a useful calving function should return this domain to stable geometry at least in terms of calving. For example, Ma et al. (2017) showed that glaciers lie within a narrow stability envelope when considering terminus thickness and water depth. Whatever the method of implementation of the calving function, unstable domains should calve back to stable positions irrespective of the initial conditions (or if stable positions are not present undergo self-sustained retreat). Regardless of whether the domain had been relaxed or not, the CD function transiently retreated to a location and glacier geometry that supported its stabilization (e.g., Figures 6 and 10). On the other hand the VM function prescribed a retreat which was either exacerbated or reduced by glacier dynamics but did not stabilize. Furthermore, the VM function did not respond directly to changes in external geometry which is known to stabilize calving (e.g., Benn et al., 2023, 2026; Bevan et al., 2019; Wheel, Benn, et al., 2024).

4.6. Comparison of Rate- and Position-Based Functions

In essence, the VM function is the ratio between terminus velocity and $\tilde{\sigma}$. Our results indicate that for a typical Greenlandic glacier, a defined increase in velocity corresponds to a greater increase in $\tilde{\sigma}$, producing a higher calving rate for higher terminus velocities. A detailed look at the 3D stress field showed the increase in $\tilde{\sigma}$ is driven by a higher magnitude of tensile stretching at the terminus. Since the CD function is tensile-stress based it seems intuitive that it would display a similar pattern, as higher terminus velocities produce a higher value of tensile stress. Yet it does not, as the distribution of the stress field remains broadly similar regardless of its magnitude. Consequently, the location of tensile stress (used to determine the position of the terminus post-calving), remains unchanged. The distinction between how the stress field is treated differently by the CD and VM functions perfectly summarizes how the choice of rate- or position-based function effects the modeled calving. In both functions changes are driven by the tensile stress, but the calving outcomes are substantially different.

Whilst the CD function responds as expected to changes in the topography, the VM function displays no change. Furthermore, there is no evidence to suggest that velocity-calving feedback displayed by the VM function exists in reality. Instead this feedback is a non-physical response which is entirely implausible and often misinterpreted as a shift in calving dynamics (e.g., Choi et al., 2018; Åkesson et al., 2022). For example, it is easy to model a situation where higher melting leads to higher terminus velocities. Using the VM function, calving would subsequently increase in what seems like a dynamic response even if the glacier was strongly pinned on a bed rock ridge.

4.7. Assessing Calving Functions

We have shown that calving rates vary over the course of a simulation and argue that this creates a source of confusion in the debate about the "best" calving function for use in ice-sheet models. Consequently, more effort should be made to assess the quality and applicability of the current range of calving functions in use. To better understand and constrain which calving functions are of use to large-scale ice-sheet simulations, we must first establish protocols to guide how a calving function can be assessed. Traditionally, calving functions are assessed by comparing tuned model results to the time taken for the glacier front to move from position A to position B (e.g., Choi et al., 2018) or to a steady state (e.g., Wilner et al., 2023). However, this method risks overfitting inappropriate functions, and takes no account of whether the calving function mirrors (on any level) how calving responds to changes in glaciological and environmental conditions. As an alternative to this fitting procedure, we propose three standards to assess the performance and usefulness of a given calving function:

1. The calving function accurately represents the calving styles of the domain,
2. Calving responds to forcings as theory dictates, capturing both stabilization and transitions in glacier dynamics, and
3. The calving function can be easily implemented and adapted for different models.

Standard 1) reflects the need for calving functions to be able to span a variety of calving styles associated with different glacial systems. For example, a calving rate function might represent the terminus movement of a tidewater glacier through continuous serac calving at some prescribed rate, whereas a glacier may calve back into a situation where the stability conditions change dramatically, and a transition to full-thickness calving occurs. Standard 2) is potentially the most useful when considering the ability of a calving function to replicate calving processes. It is important to evaluate that known responses to forcing are simulated by the calving function, for example, dynamic thinning leads to an increase in buoyant calving. This standard is important to prevent overfitting to a given glacier system or time period. Finally, the calving function must be able to capture the transitions of the glacier between stable states rather than needing to be adjusted in order to allow the glacier to retreat or advance. Standard 3) assesses whether the function can be universally implemented by different modeling groups for easy comparison.

Assuming a calving function can meet standards 1 and 2, it can be calibrated to match observed behavior, increasing confidence that any changes in internal or external forcing will be accurately reflected in future calving projections. If a calving function meets standard 3 as well, it can then be widely used for model intercomparison projects and climate models.

The CD function is frequently criticized for the lack of penetration of the modeled crevasse field especially when using an SSA-style model. It is important to note two principles of the function. First, the CD function does not physically represent the crevasse field and the term "crevasse" only refers to the envelope of extensional stress where crevasses could form. Second, the zero-stress criterion is entirely arbitrary as the model has no memory. Instead, the CD function serves as a method of parameterizing a stress field to predict calving in a continuum model. The CD function is also capable of simulating calving on grounded and ungrounded ice (e.g., Todd et al., 2018; Wheel, Benn, et al., 2024) including the tidewater glacier experiments presented here (Figure 1c). Newer modifications of the CD function such as the assessment of the horizontal force balance (e.g., Buck, 2023; Slater & Wagner, 2025) produce deeper crevasses, especially for ice shelves. However, the horizontal distribution of the stress contours will remain relatively unchanged when the zero-stress criterion is replaced with a tensile ice strength. Importantly, these methods predict where crevassing is occurring and not the rate of calving, so in the context of this paper fall under the category of position-based calving. Further advances include the addition of stochastic element as part of the CD function, which could serve as a solution for implementation at ice shelves where stresses are lower than thresholds observed for tidewater glacier setups like that presented here (Benn et al., 2026).

It is important to reflect on whether it is realistic for a simple calving function to replicate the complex calving processes to such degree as to never need any manual adjustment. This was previously the aim and proposed benefit of using the CD function in a 3D Stokes model for simulations at Store Glacier (Sermeq Kujalleq) (Cook et al., 2022; Todd et al., 2018, 2019). However, Wheel, Crawford, and Benn (2024) found that for Jakobshavn Isbrae (Sermeq Kujalleq) some adjustment to the calving criterion was required. We propose this form of adjustment of a calving function should be described as "calibration" and should remain constant between glacier states and locations. Calibration should act only as a method to overcome some of the missing processes not included within the simple calving function. This is distinct from "tuning" of calving function which we define as the manual adjustment of a calving function to fit a given glacier state or location.

5. Conclusions

We show the crevasse-depth calving function (a leading position-based calving function) can reproduce multiple calving styles from small serac events to large full-thickness calving for a typical Greenlandic glacier. By changing the ice freeboard of a synthetic tidewater glacier or changing submarine melting, the crevasse-depth function correspondingly shifts the relative proportion of serac calving to full-thickness calving. Furthermore, the crevasse-depth function can distinguish between transient and stable glacier calving states. On the other hand, the von Mises calving function (a leading rate-based calving function) displays uniform calving rates despite changes in topography or ice freeboard that are known to alter calving dynamics. Concerningly, the von Mises function displays a calving rate-velocity feedback, which is entirely unphysical and often misattributed as a dynamic calving response.

Using the crevasse-depth function, calving rates are shown to vary through time and are highly dependent on local geometry or glacier state. Calving functions must be position-based for future projections where the future state of the glacier is unknown. The rate-based function tested could not detect shifts between stable locations where calving is velocity independent. Our results indicate, rate-based functions can only replicate the calving dynamics they have been tuned to match. Calving rates are not uniform with time or glacier state.

Currently, methods for assessing calving functions are inadequate. Simple comparison of tuned model results with observed "calving rates" is not a true validation of the merits of a given calving function, but rather should be reserved only for a calibration to account for missing processes. Instead, calving functions should be more rigorously assessed using the proposed standards that (a) a calving function should accurately represent the calving styles of the domain, (b) capture stable and transient states and (c) be easily implemented. Simply, calving functions should be able to account for the key physical processes that drive calving and in doing so shifts in calving dynamics and rates will naturally emerge.

Appendix A: Synthetic Glacier Setup

The synthetic glacier is taken from Wheel, Benn, et al. (2024). It extends 5 km upstream from the calving front and has a terminus width of 3 km (Figure 1). The domain has narrowing margins and two basal rises near the terminus. Both are moved in the upstream in the geometry experiments (Figure 1e). Each simulations runs for 100 days at one day timesteps. Throughout the simulations, the domain mesh maintains a vertical and horizontal resolution at the terminus of 50 m producing a high resolution domain. The horizontal resolution increases to 500 m at the inflow boundary. For the simulations using the crevasse-depth (CD) function, the 2D PlanMesh has a resolution of 40 m. The control domain has the formulation

$$B_h(x,y) = Depth + WidthDepth + Bump1 + Bump2 + Rise, \tag{A1}$$

where

$$Depth(y) = B_0 + ym_b,\ B_0 = -550, \tag{A2}$$

$$WidthDepth(x,y) = \frac{|x-2500|}{\left(3000+\frac{y}{5}\right)} \times 400, \tag{A3}$$

$$Bump1(x,y) = \exp\left(H_b \times \frac{(x-1800)^2 + y^2}{r_b}\right)^2,\ H_b = 100,\ r_b = 550, \tag{A4}$$

$$Bump2(x,y) = \exp\left(H_b \times \frac{(x-3000)^2 + y^2}{r_b}\right)^2,\ H_b = 100,\ r_b = 550, \tag{A5}$$

$$Rise(y) = \exp\left(H_t \times \frac{-y}{l_t}\right)^2,\ H_t = 100,\ l_t = 1000, \tag{A6}$$

and where B_h is the bedrock height in meters, m_b is 1/40 the gradient of the bed, x is the x coordinate, y is the y coordinate and B_0 is the bed height at $y = 0$. For the bumps, H_b is the height of the bump and r_b is the radius of bump. The surface geometry is given by

$$S_h(y) = S_0 + ym_s,\ S_0 = 50, \tag{A7}$$

where S_h is the surface height and m_s is 1/40 the gradient of the surface.

A1. Boundary Conditions

The synthetic glacier domain featured six boundary conditions: the calving front of the glacier (Γ_{front}), the two lateral margins (Γ_{left} and Γ_{right}), the interior inflow boundary (Γ_{inflow}), the glacier base (Γ_{base}), and the top surface (Γ_{surf}). A no-penetration condition is implemented at the lateral margins of the model domain ($\Gamma_{\text{left, right}}$) since these represent the fjord walls. A simple linear friction law was imposed as a Neumann boundary condition, using a constant slip coefficient (β) of 1e−2 $MPa\ m^{-1}\ a^{-1}$. Consequently, the lateral boundary conditions are

$$u_\perp = 0, \qquad on\ \Gamma_{\text{left}}, \Gamma_{\text{right}}, \tag{A8}$$

$$\sigma_\| = -u_\| \beta, \qquad on\ \Gamma_{\text{left}}, \Gamma_{\text{right}}, \tag{A9}$$

where u denotes the velocity component and σ the stress component, with $\perp$ and $\|$ indicating the normal and tangential directions, respectively. A non-linear Weertman friction law is applied at the glacier base, using a slip coefficient of 1e−4 $MPa\ m^{-1/3}\ a^{-1/3}$ and an exponent of 3. The basal boundary condition is further complicated by the glacier's grounding line dynamics, which are treated as a contact problem following the approach of (Favier et al., 2012). When the glacier is grounded, the boundary condition resembles that of non-linear sliding, with a non-penetration constraint enforced, so

$$u_{\perp} = 0, \qquad on\ \Gamma_{\text{base}}, \tag{A10}$$

$$\sigma_{\|} = C u_b^{1/m}, \qquad on\ \Gamma_{\text{base}}, \tag{A11}$$

where C is the Weertman slip coefficient, u_b is the basal velocity and m is Weertman exponent. When the glacier is ungrounded, friction is absent, allowing free vertical motion, so

$$\sigma_{\perp} = \min(-\rho_w g h,\ 0), \qquad on\ \Gamma_{\text{base}}, \tag{A12}$$

$$\sigma_{\|} = 0, \qquad on\ \Gamma_{\text{base}}, \tag{A13}$$

where ρ_w is the density of the water, g is the gravitational acceleration and h is the depth below the water level. As with ungrounded ice, no friction is applied at the glacier's calving face. However, because it is in contact with the fjord water, a normal stress is imposed below the waterline.

$$\sigma_{\perp} = \min(-\rho_w g h,\ 0), \qquad on\ \Gamma_{\text{term}}, \tag{A14}$$

$$\sigma_{\|} = 0, \qquad on\ \Gamma_{\text{term}}. \tag{A15}$$

The inflow boundary has a fixed velocity of 1,000 ma^{-1} for the control experiments, which is assumed to be constant throughout the vertical ice column, such that

$$|\mathbf{u}| = u_{in}, \qquad on\ \Gamma_{\text{inflow}}, \tag{A16}$$

where $\mathbf{u}$ is the velocity vector and u_{in} is the inflow velocity. The surface boundary condition is stress-free. A submarine melt condition is applied at the glacier front boundary (or calving front, Γ_{term}), where a central plume and background melt are present (Figure 1b). The plume is based on summer plume simulations by Kajanto et al. (2023) for Ilulissat Fjord. To adapt it to the synthetic domain-where the maximum flow velocity is 1,500 ma^{-1}, significantly slower than the 10,000 ma^{-1} observed at Jakobshavn Isbrae (Sermeq Kujalleq) - the plume profile was normalized. The maximum plume melt was set to 500 ma^{-1}, and the profile scaled accordingly. No melt was applied to the underside of the floating ice.

Appendix B: Calving Size Frequency Distributions

Populations of icebergs can be expressed using generic fragment size distributions (Åström et al., 2021). This can be expressed as

$$n(S) = c_1 S^{-\alpha} \exp(-S/S_1) + c_2 \exp(-S/S_2) \tag{B1}$$

where α is derived from the universal fracture processes in elastic-brittle materials, n is the relative abundance of a size-interval (S), c_1 and c_2 are constants, and the characteristic size intervals of a specific fracture process is defined by S_1 and S_2. The first term of the right hand side of the equation generates to a power law distribution that can describe serac calving size distributions and the second term produces an exponential distribution which characterizes the distribution of full-thickness calving events (Benn et al., 2026; Åström et al., 2021).

Conflict of Interest

The authors declare no conflicts of interest relevant to this study.

Availability Statement

The Elmer calving model is maintained and available (Ruokolainen et al., 2023). The experimental setups, data analysis scripts, terminus and calving outputs are available (Wheel, 2025).

Acknowledgments

This work is from the DOMINOS project, a component of the International Thwaites Glacier Collaboration (ITGC). This work has received support from the Natural Environmental Research Council (NERC; Grant NE/006605/1) and the Advanced Research + Invention Agency (ARIA) Forecasting Tipping Points programme (GIANT project; SCOP-PR01-P028). GIANT Contribution No. GIANT-001. ITGC Contribution No. ITGC-175. A.J.C. was supported by the Royal Society (RG \R1\251361) and Royal Society of Edinburgh Personal Research Fellowship programme.

References

Åkesson, H., Morlighem, M., Nilsson, J., Stranne, C., & Jakobsson, M. (2022). Petermann ice shelf may not recover after a future breakup. *Nature Communications*, *13*(1), 2519. https://doi.org/10.1038/s41467-022-29529-5

Alley, R. B., Cuffey, K. M., Bassis, J. N., Alley, K. E., Wang, S., Parizek, B. R., et al. (2023). Iceberg calving: Regimes and transitions. *Annual Review of Earth and Planetary Sciences*, *51*(1), 189–215. https://doi.org/10.1146/annurev-earth-032320-110916

Åström, J., Cook, S., Enderlin, E. M., Sutherland, D. A., Mazur, A., & Glasser, N. (2021). Fragmentation theory reveals processes controlling iceberg size distributions. *Journal of Glaciology*, *67*(264), 603–612. https://doi.org/10.1017/jog.2021.14

Åström, J., Riikilä, T. I., Tallinen, T., Zwinger, T., Benn, D., Moore, J. C., & Timonen, J. (2013). A particle based simulation model for glacier dynamics. *The Cryosphere*, *7*(5), 1591–1602. https://doi.org/10.5194/tc-7-1591-2013

Benn, D. I., & Åström, J. A. (2018). Calving glaciers and ice shelves. *Advances in Physics X*, *3*(1), 1048–1076. https://doi.org/10.1080/23746149.2018.1513819

Benn, D. I., Hulton, N. R., & Mottram, R. H. (2007). Calving laws, sliding laws and the stability of tidewater glaciers. In *Annals of Glaciology* (Vol. 46, pp. 123–130). Cambridge University Press. https://doi.org/10.3189/172756407782871161

Benn, D. I., Todd, J., Luckman, A., Bevan, S., Chudley, T. R., Åström, J., et al. (2023). Controls on calving at a large Greenland tidewater glacier: Stress regime, self-organised criticality and the crevasse-depth calving law. *Journal of Glaciology*, *69*(278), 2059–2074. https://doi.org/10.1017/jog.2023.81

Benn, D. I., Wheel, I., Åström, J., Christoffersen, P., Cook, S. J., Luckman, A., et al. (2026). Calving laws and where to find them. *Journal of Glaciology*, *72*, 1–35. https://doi.org/10.1017/jog.2026.10128

Bevan, S. L., Luckman, A. J., Benn, D. I., Cowton, T., & Todd, J. (2019). Impact of warming shelf waters on ice mélange and terminus retreat at a large se Greenland glacier. *The Cryosphere*, *13*(9), 2303–2315. https://doi.org/10.5194/tc-13-2303-2019

Bézu, C., & Bartholomaus, T. C. (2024). Greenland ice sheet's distinct calving styles are identified in terminus change timeseries. *Geophysical Research Letters*, *51*(21), e2024GL110224. https://doi.org/10.1029/2024GL110224

Bondzio, J. H., Seroussi, H., Morlighem, M., Kleiner, T., Rückamp, M., Humbert, A., & Larour, E. Y. (2016). Modelling calving front dynamics using a level-set method: Application to Jakobshavn Isbræ, West Greenland. *The Cryosphere*, *10*(2), 497–510. https://doi.org/10.5194/tc-10-497-2016

Buck, W. R. (2023). The role of fresh water in driving ice shelf crevassing, rifting and calving. *Earth and Planetary Science Letters*, *624*(October), 118444. https://doi.org/10.1016/j.epsl.2023.118444

Cassotto, R. K., Burton, J. C., Amundson, J. M., Fahnestock, M. A., & Truffer, M. (2021). Granular decoherence precedes ice mélange failure and glacier calving at Jakobshavn Isbræ. *Nature Geoscience*, *14*(6), 417–422. https://doi.org/10.1038/s41561-021-00754-9

Choi, Y., Morlighem, M., Wood, M., & Bondzio, J. H. (2018). Comparison of four calving laws to model Greenland outlet glaciers. *The Cryosphere*, *12*(12), 3735–3746. https://doi.org/10.5194/tc-12-3735-2018

Cook, S. J., Christoffersen, P., & Todd, J. (2022). A fully-coupled 3D model of a large Greenlandic outlet glacier with evolving subglacial hydrology, frontal plume melting and calving. *Journal of Glaciology*, *68*(269), 486–502. https://doi.org/10.1017/jog.2021.109

Crawford, A., Åström, J., Benn, D. I., Luckman, A., Gladstone, R., Zwinger, T., et al. (2024). Calving dynamics and the potential impact of mélange buttressing at the Western calving front of thwaites Glacier, West Antarctica. *Journal of Geophysical Research: Earth Surface*, *129*(10), e2024JF007737. https://doi.org/10.1029/2024JF007737

Duddu, R., Jiménez, S., & Bassis, J. (2020). A non-local continuum poro-damage mechanics model for hydrofracturing of surface crevasses in grounded glaciers. *Journal of Glaciology*, *66*(257), 415–429. https://doi.org/10.1017/jog.2020.16

Favier, L., Gagliardini, O., Durand, G., & Zwinger, T. (2012). A three-dimensional full Stokes model of the grounding line dynamics: Effect of a pinning point beneath the ice shelf. *The Cryosphere*, *6*(1), 101–112. https://doi.org/10.5194/tc-6-101-2012

Fried, M. J., Catania, G. A., Stearns, L. A., Sutherland, D. A., Bartholomaus, T. C., Shroyer, E., & Nash, J. (2018). Reconciling drivers of seasonal terminus advance and retreat at 13 central west Greenland tidewater glaciers. *Journal of Geophysical Research: Earth Surface*, *123*(7), 1590–1607. https://doi.org/10.1029/2018JF004628

Gagliardini, O., Zwinger, T., Gillet-Chaulet, F., Durand, G., Favier, L., De Fleurian, B., et al. (2013). Capabilities and performance of Elmer/Ice, a new-generation ice sheet model. *Geoscientific Model Development*, *6*(4), 1299–1318. https://doi.org/10.5194/gmd-6-1299-2013

Goliber, S. A., & Catania, G. A. (2024). Glacier Terminus morphology informs calving style. *Geophysical Research Letters*, *51*(15), 1–11. https://doi.org/10.1029/2024GL108530

Huth, A., Duddu, R., & Smith, B. (2021). A generalized interpolation material point method for shallow ice shelves. 2: Anisotropic nonlocal damage mechanics and rift propagation. *Journal of Advances in Modeling Earth Systems*, *13*(8), 1–26. https://doi.org/10.1029/2020MS002292

Huth, A., Duddu, R., Smith, B., & Sergienko, O. (2023). Simulating the processes controlling ice-shelf rift paths using damage mechanics. *Journal of Glaciology*, *69*(278), 1915–1928. https://doi.org/10.1017/jog.2023.71

IPCC. (2023). IPCC, 2023: Summary for policymakers. In H. L. Core Writing Team (Ed.), *Climate change 2023: Synthesis report. A report of the intergovernmental panel on climate change. contribution of working groups I, II, and III to the sixth assessment report of the intergovernmental panel on climate change*. IPCC

Joughin, I., Shean, E., Smith, B., & Floricioiu, D. (2020). A decade of variability on Jakobshavn Isbræ: Ocean temperatures pace speed through influence on mélange rigidity. *The Cryosphere*, *14*(1), 211–227. https://doi.org/10.5194/tc-14-211-2020

Kajanto, K., Straneo, F., & Nisancioglu, K. (2023). Impact of icebergs on the seasonal submarine melt of Sermeq Kujalleq. *The Cryosphere*, *17*(1), 371–390. https://doi.org/10.5194/tc-17-371-2023

Levermann, A., Albrecht, T., Winkelmann, R., Martin, M. A., Haseloff, M., & Joughin, I. (2012). Kinematic first-order calving law implies potential for abrupt ice-shelf retreat. *The Cryosphere*, *6*(2), 273–286. https://doi.org/10.5194/tc-6-273-2012

Ma, Y., Tripathy, C. S., & Bassis, J. N. (2017). Bounds on the calving cliff height of marine terminating glaciers. *Geophysical Research Letters*, *44*(3), 1369–1375. https://doi.org/10.1002/2016GL071560

Mercenier, R., Lüthi, M. P., & Vieli, A. (2019). A transient coupled ice flow-damage model to simulate iceberg calving from tidewater outlet glaciers. *Journal of Advances in Modeling Earth Systems*, *11*(9), 3057–3072. https://doi.org/10.1029/2018MS001567

Morlighem, M., Bondzio, J., Seroussi, H., Rignot, E., Larour, E., Humbert, A., & Rebuffi, S. (2016). Modeling of Store Gletscher's calving dynamics, West Greenland, in response to ocean thermal forcing. *Geophysical Research Letters*, *43*(6), 2659–2666. https://doi.org/10.1002/2016GL067695

Nick, F. M., Van Der Veen, C. J., Vieli, A., & Benn, D. I. (2010). A physically based calving model applied to marine outlet glaciers and implications for the glacier dynamics. *Journal of Glaciology*, *56*(199), 781–794. https://doi.org/10.3189/002214310794457344

O'Leary, M., & Christoffersen, P. (2013). Calving on tidewater glaciers amplified by submarine frontal melting. *The Cryosphere*, *7*(1), 119–128. https://doi.org/10.5194/tc-7-119-2013

Ranganathan, M., Robel, A. A., Huth, A., & Duddu, R. (2025). Glacier damage evolution over ice flow timescales. *The Cryosphere*, *19*(4), 1599–1619. https://doi.org/10.5194/tc-19-1599-2025

Ruokolainen, J., Malinen, M., Råback, P., Zwinger, T., Takala, E., Kataja, J., et al. (2023). Elmercsc/elmerfem: Elmer 9.0 [Software]. *Zenodo*. https://doi.org/10.5281/zenodo.7892181

Slater, D. A., & Wagner, T. J. (2025). Calving driven by horizontal forces in a revised crevasse-depth framework. *The Cryosphere*, *19*(7), 2475–2493. https://doi.org/10.5194/tc-19-2475-2025

Sun, S., Cornford, S. L., Moore, J. C., Gladstone, R., & Zhao, L. (2017). Ice shelf fracture parameterization in an ice sheet model. *The Cryosphere*, *11*(6), 2543–2554. https://doi.org/10.5194/tc-11-2543-2017

Todd, J., Christoffersen, P., Zwinger, T., Räback, P., & Benn, D. I. (2019). Sensitivity of a calving glacier to ice-ocean interactions under climate change: New insights from a 3-d full-stokes model. *The Cryosphere*, *13*(6), 1681–1694. https://doi.org/10.5194/tc-13-1681-2019

Todd, J., Christoffersen, P., Zwinger, T., Råback, P., Chauché, N., Benn, D. I., et al. (2018). A full-stokes 3-D calving model applied to a large Greenlandic Glacier. *Journal of Geophysical Research: Earth Surface*, *123*(3), 410–432. https://doi.org/10.1002/2017JF004349

Vallot, D., Adinugroho, S., Strand, R., How, P., Pettersson, R., Benn, D. I., & Hulton, N. R. (2019). Automatic detection of calving events from time-lapse imagery at Tunabreen, Svalbard. *Geoscientific Instrumentation, Methods and Data Systems*, *8*(1), 113–127. https://doi.org/10.5194/gi-8-113-2019

Vieli, A., Funk, M., & Blatter, H. (2001). Flow dynamics of tidewater glaciers: A numerical modelling approach. *Journal of Glaciology*, *47*(159), 595–606. https://doi.org/10.3189/172756501781831747

Wheel, I. (2025). Emergent dynamics from a position-based calving law and the limits of rate-based calving laws [Dataset]. *Zenodo*. https://doi.org/10.5281/zenodo.17404544

Wheel, I., Benn, D. I., Crawford, A. J., Todd, J., & Zwinger, T. (2024). A new 3D full-stokes calving algorithm within Elmer/Ice (v9.0). *Geoscientific Model Development*, *17*(14), 5759–5777. https://doi.org/10.5194/gmd-17-5759-2024

Wheel, I., Crawford, A. J., & Benn, D. I. (2024). Calving dynamics at Jakobshavn Isbrae (Sermeq Kujalleq) controlled by local geometry: Insights from a 3D stokes calving model. *Journal of Glaciology*, *70*, e7. https://doi.org/10.1017/jog.2024.77

Wilner, J. A., Morlighem, M., & Cheng, G. (2023). Evaluation of four calving laws for Antarctic ice shelves. *The Cryosphere*, *17*(11), 4889–4901. https://doi.org/10.5194/tc-17-4889-2023

Wolper, J., Gao, M., Lüthi, M. P., Heller, V., Vieli, A., Jiang, C., & Gaume, J. (2021). A glacier–ocean interaction model for tsunami genesis due to iceberg calving. *Communications Earth & Environment*, *2*(1), 1–10. https://doi.org/10.1038/s43247-021-00179-7

Zarrinderakht, M., Schoof, C., & Peirce, A. (2024). An analysis of the interaction between surface and basal crevasses in ice shelves. *The Cryosphere*, *18*(8), 3841–3856. https://doi.org/10.5194/tc-18-3841-2024